Microwave Tomographic Inversion Technique Based on Stochastic Approach for Rainfall Fields Monitoring

Dino Giuli, *Senior Member, IEEE*, Luca Facheris, *Member, IEEE*, and Simone Tanelli *Member, IEEE*

Abstract— The microwave tomographic inversion technique (MTIT) proposed in 1991 for reconstruction of rainfall fields at ground through microwave attenuation measurements is reconsidered here. A new algorithm for data inversion is presented [referred to as stochastic reconstruction technique (SRT)] that generally performs better than the one originally adopted [referred to as arithmetic reconstruction technique (ART)]. Improvement is achieved in spatial definition and general reliability of rainfall field reconstruction. The new model adopted to represent the reconstructed rainfall fields leads to a completely different strategy for the inversion problem, and this strategy is based on a global optimization stochastic technique (GOST). Results obtained through the SRT-MTIT are presented in the paper and compared to those obtained by employing the ART-MTIT. It also is shown that, based on the SRT-MTIT approach, fast and reliable time tracking of rainfall events is made possible by exploiting previous reconstructions and by the improved long-term physical consistency of the model adopted for rainfall field decomposition.

Index Terms— Attenuation measurements, rainfall, tomography, tracking.

NOMENCLATURE

ATA	Adapted timmer algorithm; ATA1: version 1, ATA2: version 2.
ART	Arithmetic reconstruction technique.
DRT	Dynamic reconstruction technique.
GOST	Global optimization stochastic technique.
MAS	Master analysis and stop.
MSE	Mean-square error.
MTIT	Microwave tomographic inversion technique.
NMSE	Normalized mean-square error.
PC	Pseudo cell.
PSS	Progressive stochastic search.
RS	Random solution.
RSS	Random solutions selector.
RSO	Random solutions optimizer.
SRT	Stochastic reconstruction technique.

I. INTRODUCTION

UNTIL THE 1980's, research on atmospheric rainfall monitoring evolved with the basic purpose of developing increasingly sophisticated models of atmospheric events. Data obtained either by direct measurements through *in-situ* sensors (e.g., raingauges) or by remote sensing (e.g., through weather radars and spaceborne sensors) helped to develop effective and complex theories. These in turn increased the reliability of the data analysis process and the predictive algorithms utilized mainly at the mesoscale or synoptic scale level [1]. Omitting the different opinions about specific issues of rainfall fields monitoring, the rainfall process can be regarded both locally and instantaneously as a random process with a highly variable component (fluctuations with "atom at zero" distribution) superimposed on a more stable component (intensity component averaged over the small mesoscale) [2]. Indeed, the main problems in remote sensing of atmospheric events are related strictly to their complex spatial and temporal dynamics and to the high number of varying factors by which they are influenced (e.g., thermodynamic factors, orography, etc.). Clear evidence of this was given through weather radar data analysis [3].

At the same time, the demand also increased for reliable data at smaller scales (the so-called meso-β and meso-γ scales [4]) and with enhanced time resolution capability (some minutes). Implementation of monitoring systems for the reduction of the hydrogeological hazard has been urged by several environmental disasters caused by events of remarkable intensity. Nevertheless, fully effective means of data acquisition at the meso-β and meso-γ scale are lacking. The consequence is a lack of basic knowledge in many areas, one of which is the structure of rainfall events that occur and develop over mountainous areas.

In this framework, a small-scale rainfall monitoring system, an alternative to classical raingauge networks and weather radars, was described and studied for the first time in [5]. The basic idea was to exploit the correlation between the specific attenuation K affecting the electromagnetic (e.m.) waves propagating in rainfall and the rainfall intensity R. Total attenuation measurements made along multiple terrestrial paths forming a network then could be exploited to provide an estimate of the rainfall field over the area containing that network. Centimeter wavelengths were considered, for which the uncertainties in the K–R relationships do not exceed approximately 10%. In particular, simulations were carried

out at 35 GHz, where such relationships are quasilinear and particularly accurate. Due to sensitivity requirements posed by the receiver apparatus, each microwave path in such a system should not be longer than 15 km. Therefore, the small mesoscale characteristics prevail in the estimated mean values of rainfall. The primary objective of the network is to single out the basic features of the cells (namely the mesoscale features) in the monitored area. The reason is twofold. The first is to pursue reliable estimates of the average rainfall intensity over the area, and the second is to obtain useful information for both classification and tracking purposes.

In Section II of this paper, for ease of reference, we briefly recall the basic tomographic principle discussed in [5]. In Section III-A, the specific MTIT proposed in that paper and here referred to as MTIT-ART is briefly recalled. The limitations posed by that deterministic approach to the particular tomographic inversion problem at hand and the related problems are then highlighted as introductory to the matter of this paper. The exclusive objective is the definition of a more efficient and robust strategy of reconstruction and tracking of rainfall fields, based on a stochastic solution search technique and followed by a finite sequence of optimization and control phases. In Sections III-B and C, we describe such a new approach, referred to as SRT-MTIT, first justifying the choices that serve as keys to overcoming the problems left unsolved by the ART-MTIT and then illustrating in better detail the way followed to face the new problems posed by such choices.

In Section IV, we introduce the DRT, a technique for tracking rainfall fields based on the SRT-MTIT and show that the increased flexibility and physical consistency of the reconstruction model and strategy are ground premises for faster and more reliable tracking of rainfall events. Finally, in Section V, we report on some selected results obtained via simulations. These were carried out on rainfall fields converted from radar reflectivity data collected by the POLAR 55C radar (Montagnana-Firenze) [6]. While comparing the ART, SRT, and DRT reconstructions and discussing performance parameters, the analysis of the real event gives the opportunity to get a better insight into some specific reconstruction problems and anomalies that may occur and to better understand the advantages of the new technique.

II. PRINCIPLE OF MICROWAVE ATTENUATION TOMOGRAPHY

Assuming a plane horizontal surface and an x–y Cartesian coordinate system, let us define $R(x, y, t)$ as the rainfall intensity field at ground at a given instant t. The corresponding specific attenuation field $K(x, y, t)$ is theoretically defined through well-known empirical relationships of the kind

$$K = aR^b \qquad (1)$$

where K is expressed in dB/km and R in mm/h. For the frequency $f = 35$ GHz, experimental data give $a = 0.221$ and $b = 1.04$ with an average error smaller than 10% (see [7], [8]).

Given one transmitting and one receiving station at ground, operating at microwaves while separated several kilometers from each other, it is possible to estimate the average rainfall intensity along the propagation path through total attenuation
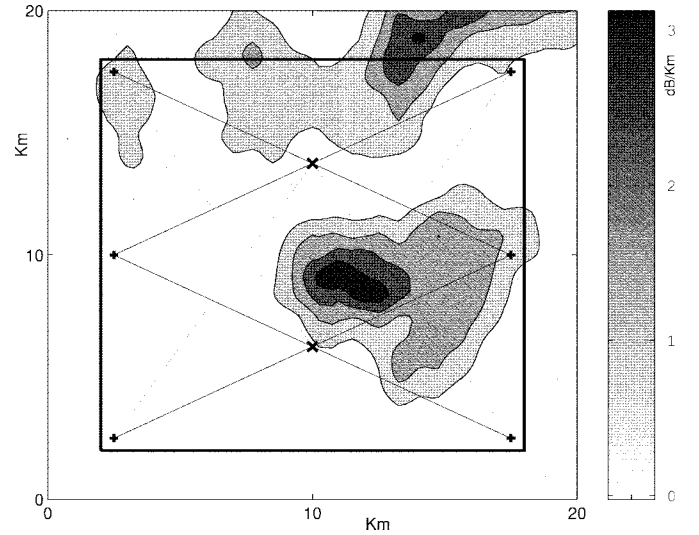

Fig. 1. Two–dimensional (2-D) distribution of the specific attenuation as derived from a radar-monitored event (November 10, 1994). Transmitters and receivers of the tomographic system are evidenced by the "+" and "×" symbols, respectively. The black square indicates the area (A_R) where the tomographic reconstruction is evaluated.

measurements [3]. If an area of interest with a surface of a few hundred km^2 is covered by a set of microwave links as shown in Fig. 1, several path attenuation measurements can be made simultaneously. It is then possible to pursue a sort of tomographic inversion to retrieve $K(x, y, t)$ and in turn $R(x, y, t)$. Considering that the time needed to perform attenuation measurements can be remarkably shorter than the evolution time of the rainfall process, the reconstruction is practically instantaneous. The term "tomographic inversion" is appropriate, since the objective is the retrieval of an instantaneously measured, two-dimensional (2-D) field, based on several one-dimensional (1-D) average measurements.

A complete survey of the error sources affecting the measurement of, and the uncertainties in, the K–R relationship is available in [5]. In the same paper, the advantages of a microwave tomographic system are enumerated, and they are compared in particular with regard to problems and technological requirements posed by a weather radar station in some operational conditions. Several possible important applications of such a system also were cited, ranging from its basic utilization in narrow but important orographic basins, possibly out of radar coverage, to its integration in a network of radar and raingauges for integration and/or calibration and validation of data collected by different sensors. In this paper, we deal exclusively with the inversion problem strategy, and the reader is referred to [5] for a discussion of the aforementioned operational issues and for feasibility (and cost) analysis.

Assuming that the transmitters' antenna beamwidths are sufficiently narrow, the propagation path can be considered a straight line. Thus, the attenuation (in decibels) that the e.m. wave undergoes along a given link is

$$m = \frac{\int_{t_0}^{t_f} \int_{r_T}^{r_R} K(r, t)\, dr\, dt}{t_f - t_0} \qquad (2)$$

where $K(r,t)$ is the specific attenuation at the range $r = \sqrt{(x^2 + y^2)}$ (along the transmission path) at time t, while r_T and r_R are the transmitter and receiver ranges, respectively ($[t_0 \, t_f]$ being the time observation interval).

Once a network topology is given, i.e., a set of transmitter–receiver links is arranged in the x-y plane and N_p microwave paths are consequently defined, two vectors also can be defined as follows.

m Path measurement data vector (size N_p) actually observed. Its ith component m_i is the total attenuation measured along the ith link of the network. In simulations, it can be computed through (2) using the assumed true specific attenuation field $K(x,y,t)$.

$\hat{m}$ Estimated path measurement data vector (size N_p). Its ith component is the total attenuation along the ith link of the network as provided by (2), using the estimated specific attenuation field generated by the reconstruction algorithm.

Before illustrating two different MTIT's, it is opportune to point out two basic assumptions exploited in the following.

1) An operating frequency of 35 GHz is used because of the quasilinearity and the good accuracy characterizing (1) under this assumption (see [8]). The quasilinear relationship allows it to deal directly with the reconstruction of the $R(x,y,t)$ field, rather than the $K(x,y,t)$ field, neglecting the problem of a linear conversion from K to R that is not perfect.

2) In simulations and evaluations, we talk about "static" reconstructions and "instantaneous" evaluations for convenience, while in actuality we are referring to reconstructions and evaluations averaged over a time basis of some seconds (typically 30 s.).

III. Two Approaches to the Microwave Attenuation Tomographic Reconstruction Problem

In real cases, spatial and temporal dynamics of rainfall evidently do not allow the monitoring system outlined in Section II to provide complete information about the structure and development of the rainfall field. Moreover, any MTIT leads to a nontrivial problem of inversion. In fact, it is by far impossible, from a practical point of view, to increase the number of links and to arrange them to "cover" the monitored area as, for instance, in biomedical applications. The behavior of the measuring system resembles that of a low-pass filter with a band that is too narrow with respect to that of the signal of interest, and consequently, the observed data are far from being optimally sampled. Thus, robust reconstruction techniques are needed in order to achieve estimates of the average rainfall rate and basic rainfall field patterns that are of some significance for applications.

In this paragraph, two different inversion approaches are considered. The first is that originally proposed in [5], and the second, proposed in this paper, is based on a radically different strategy, suggested by accurate investigation of typical behaviors of the original method.
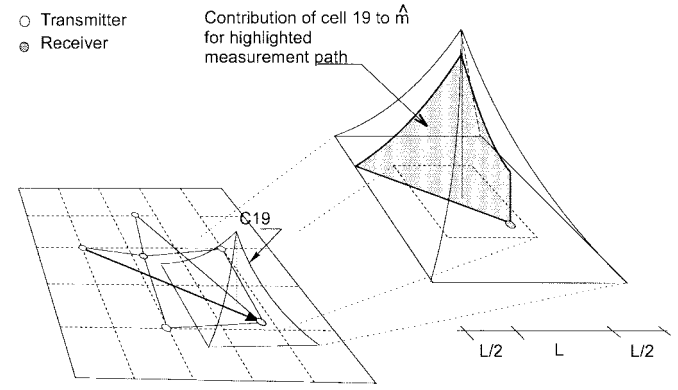

Fig. 2. Sketch of the ART basis function grid and of the contribution of one cell to the estimated path attenuation measurement ($\hat{m}$).

A. Discrete Model and the ART Inversion Approach

The discrete model proposed in [5] and briefly outlined here is based on the subdivision of the monitored square region in N identical $\Delta \times \Delta$ square subareas, where N is fixed *a priori*. The reconstructed rainfall field is expressed as a linear combination of N basis functions, each placed in the middle of a subarea (see Fig. 2) and defined as follows:

$$\psi_i(x,y) = \Lambda\left(\frac{x - X_i}{\Delta}\right)\Lambda\left(\frac{y - Y_i}{\Delta}\right), \quad i = 1, 2, \cdots, N \tag{3}$$

where

$$\Lambda(u) = \begin{cases} 1 - |u|, & \text{for } -1 \leq u \leq 1 \\ 0, & \text{elsewhere} \end{cases} \tag{4}$$

and (X_i, Y_i) are the center coordinates of the ith subarea. Notice that the basis functions are nonzero on a finite domain (with area $2\Delta \times 2\Delta$), covering nine grid cells. The reconstructed (estimated) rainfall field $\hat{R}(x,y)$ is then given by

$$\hat{R}(x,y;\boldsymbol{s}) = \sum_i^N s_i \cdot \psi_i(x,y) \tag{5}$$

where we evidenced the dependence on the expansion coefficients vector $\boldsymbol{s} = (s_1, s_2, \cdots s_N)$.

In this approach, given a set of N_p attenuation measurements, the problem posed is to find the optimum set of elements of s, denoted as s' that meets the following conditions:

$$\boldsymbol{s}': J(\boldsymbol{s}';\boldsymbol{m}) = \min_{s} J(\boldsymbol{s};\boldsymbol{m}) \tag{6}$$

with

$$J(\boldsymbol{s};\boldsymbol{m}) = \tfrac{1}{2}\,\boldsymbol{s}^T(\boldsymbol{I} + b_0\boldsymbol{B})\boldsymbol{s} + \tfrac{1}{2}a_0\|\boldsymbol{m} - \hat{\boldsymbol{m}}(\boldsymbol{s})\|^2 \tag{7}$$

where

$\boldsymbol{I}$ unitary $N \times N$ matrix;

b_0, a_0 two weighting parameters; Their tuning is a main issue for the application of this technique.

$\boldsymbol{B}$ the $N \times N$ matrix to weigh the correlations among the expansion coefficients of neighboring cells (first proposed in [9]);

$\|\boldsymbol{m} - \hat{m}(\boldsymbol{s})\|^2$ the quadratic error between the observed data vector $\boldsymbol{m}$ (made up by the real N_p attenuation measurements) and the estimated data vector $\hat{m}(\boldsymbol{s})$ (computed by means of (2) applied on $\hat{K}(x, y, t)$).

Notice that J is the standard MSE functional plus two additional terms. They were included to ensure the convergence of the inversion algorithm, since the posed inversion problem is underconstrained. The first term $(\frac{1}{2}\boldsymbol{s}^T\boldsymbol{s})$ is the quadratic dispersion of the components of $\boldsymbol{s}$, while the second one $(\frac{1}{2}\boldsymbol{s}^T\boldsymbol{B}\boldsymbol{s})$ is the weighted local variation of such expansion coefficients (see [9]). Then, an iterative algorithm, first proposed in [10], was employed to solve the optimization problem (minimization of J).

Such a technique belongs to the ART's [11]. Its behavior was investigated in depth, and the following basic conclusions were drawn in [5]:

1) performance of the ART-MTIT were compared to that obtainable through a telemetered raingauge network of comparable efficiency, exploiting the classical topo-hyets method. The former led to significantly better results, in particular when considering the average rainfall estimates over the monitored area. Nevertheless, the iterative approach poses the problem of the speed of convergence to stable solutions and also some spatial resolution problems;

2) spatial resolution problems primarily are related to the rigid definition of the grid. In fact, the rainfall field is reproduced with an intrinsic resolution that evidently is related to the grid cell size. Even if it were possible from a practical point of view, the cell size could not be indefinitely reduced to increase the resolution. In fact, due to the complexity of the system to be solved, increasing the number of subareas often leads to insurmountable problems of convergence instead of bringing significant improvements in reconstruction accuracy (see [5] and [12]). Furthermore, a deformation of the reconstructed field often was observed with respect to the original, due to the rigid positioning of the basis functions. It also was evidenced that the deformation depends on the network topology;

3) two temporally subsequent reconstructions do not always exhibit a significant correlation. In fact, in some particular situations, the deterministic approach used by ART-MTIT to solve the ill-conditioned inversion problem is not locally stable, in the sense that small perturbations applied to the observed data lead to "optimal" vectors s with a few radically different components;

4) more complex monitoring networks in principle may bring some advantage in terms of MSE. Nevertheless, the aforementioned limitation in spatial resolution limits in turn make such improvements possible [13].

B. Continuous Model for the SRT Approach

The new MTIT approach that is the main subject of this paper is based on a radically different model of the reconstructed rainfall fields. Its definition was inspired by the convinction that the main problems left unsolved by the ART-MTIT approach are primarily due to the discrete model on which it is based.

In the new approach, referred to as SRT-MTIT in the following, the reconstructed rainfall field is still expressed by a linear combination of basis functions weighted by the expansion coefficients vector s as defined in Section III-A

$$\hat{R}(x, y; \boldsymbol{s}) = \sum_{i=1}^{N} s_i \cdot h_i(x, y). \qquad (8)$$

However, differently from the discrete model, the basis functions are 2-D Gaussian symmetric functions, referred to as PC's for the reason mentioned later in point 2

$$h_i(x, y) = h(\rho_i, W_i) = \frac{1}{\sqrt{2\pi}} \exp\left(\frac{-\rho_i^2}{2W_i^2}\right)$$
$$\rho_i = \sqrt{(x - X_i)^2 + (y - Y_i)^2}, \qquad i = 1, 2, \cdots, N \quad (9)$$

where (X_i, Y_i) km are the center coordinates of the ith basis functions, while W_i km is related to the cell width.

The central simmetry of the Gaussian-shaped PC allows the fast computation of its contribution to $\hat{m}$. In fact, the contribution of one PC to the line integral along a segment connecting two points $(X_i^{\mathrm{TR}}, Y_i^{\mathrm{TR}})$ and $(X_i^{\mathrm{REC}}, Y_i^{\mathrm{REC}})$, representing the two ends of the measurement path, can be factorized through two 1-D functions (see also Fig. 3). The first one depends on the PC's width W_i and the distance $d_{i,j}$ between the ith PC's center and the jth path. The second one depends on W_i and on the two complementary lengths $R_{i,j}$ and $T_{i,j}$ (refer to Fig. 3)

$$K_{i,j} = \frac{s_i W_i}{2} e^{(-d_{i,j}^2/2W_i^2)} \left[\mathrm{erf}\left(\frac{R_{i,j}}{\sqrt{2}W_i}\right) - \mathrm{erf}\left(\frac{T_{i,j}}{\sqrt{2}W_i}\right)\right]$$
$$i = 1, 2, \cdots, N_{\mathrm{PC}}, \qquad j = 1, 2, \cdots, N_p \quad (10)$$

where

$$\mathrm{erf}(x) = \frac{2}{\sqrt{\pi}} \int_0^x e^{-x^2} dz. \qquad (11)$$

This is a decisive issue given the number of PC samplings needed to search for the solution. Furthermore, the following main differences must be pointed out, compared to the ART-MTIT approach.

1) The 2-D Gaussian shape grants continuity of all derivatives of the rainfall field for any linear combination of the elementary cells. Thus, the contribution of attenuation along a link due to a basic function always varies smoothly when its parameters undergo small variations. This helps to overcome point c) of Section III-A.

2) The 2-D Gaussian shape intrinsically adds some physical significance (in a statistical sense) to the reconstructed fields. In fact, though real rain cells do not have a well-defined shape (thus, any shape could be considered equivalent to the other in principle), long term statistics of rainfall over an extended area can be well described through elementary Gaussian cells (see [14]). Therefore, while the typical low resolution of MTIT static reconstructions makes the choice of the cell shape irrelevant to the appearance of reconstructed rain fields, such shape
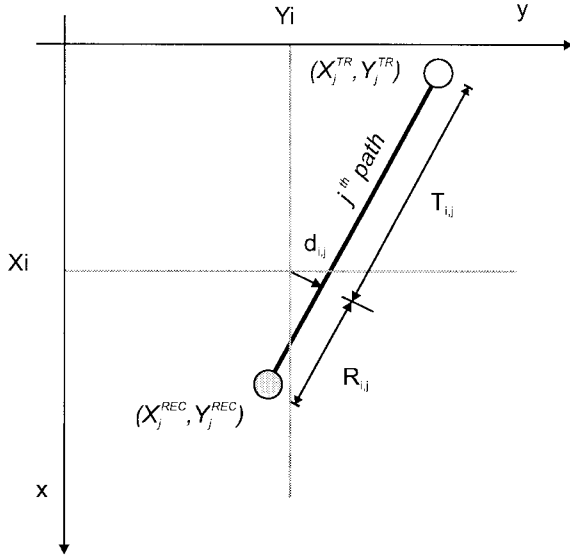
Fig. 3.   Distance parameters involved in the computation of (10).

becomes important when reconstructing cumulated rain-fall distribution over the area. As shown in Section V, SRT-MTIT outperforms the ART-MTIT when applied to the dynamic tracking of rainfall.

3) As in the ART, the $h_i(x,y)$ functions in the expansion formula of (8) do not constitute an orthogonal basis for the reconstruction and hence, the uniqueness of the solution is not guaranteed. The difference with the ART is that the correlation among two or more basis functions is not limited by constraints on their mutual positions. This is one of the most important issues that have been accounted for when developing the SRT. In fact, though such lack of constraint on the positions of the basis functions set requires a more careful approach for ensuring convergence to the solution, it also grants more insensitivity to measurement uncertainties [15].

4) In the ART-MTIT, the expansion coefficient vector weighs a set of basis functions whose number N, position (X_i, Y_i), and width Δ are rigidly defined *a priori*. On the contrary, in this model, the number of cells (hereafter referred to as N_{PC}) and the parameters X_i, Y_i and W_i must be determined jointly with s.

Solution Search Domain: Consider the $N_{PC} \times 4$ array defined as follows:

$$a = \begin{bmatrix} a_1 \\ a_2 \\ \vdots \\ a_{N_{PC}} \end{bmatrix} = \begin{bmatrix} s_1 & X_1 & Y_1 & W_1 \\ s_2 & X_2 & Y_2 & W_2 \\ \vdots & \vdots & \vdots & \vdots \\ s_{N_{PC}} & X_{N_{PC}} & Y_{N_{PC}} & W_{N_{PC}} \end{bmatrix}. \quad (12)$$

Each row of a fully defines one PC. The four entries of the ith row can take any value in intervals that define the search domain for the ith PC. Such a search domain will be hereafter referred to as A_i^4, a hyper-rectangle in $\Re^4$. While every A_i^4 is adjusted during the search process, the following practical considerations can help to define their initial settings.

1) Since the ith PC must affect at least one path-integrated attenuation measurement significantly, the center coor-

dinates X_i and Y_i must lie within the monitored area or in its neighborhood.

2) The minimum value of the width W_i depends on the spatial resolution that is intrinsically determined by the measurement network. A higher resolution allows a lower minimum value of W_i. Nevertheless, this never can be smaller than 0.5 km, here assumed as the minimum size of a rain cell. Instead, no maximum value of W_i is set *a priori*. In fact, a nearly constant rainfall field covering the monitored area is well represented by a very wide cell.

3) The range of s_i can be chosen, referring to long-term statistics of the minimum and maximum rainfall intensities over the monitored area.

C. SRT Inversion Approach

1) Error Functional in the SRT: Evidently, the new model in itself can not solve the aforementioned intrinsic problems of underconditioning. Moreover, the extent and the continuity of the solutions' domain is a major problem for convergence to reliable solutions. The main difficulty is searching for the global minimum of the error functional.

Despite this undeniable complication, a greater flexibility is brought by the continuity of the parameter values of the PC. In fact, the continuous model, used jointly with a GOST [16], is expected to overcome the ART-MTIT limitations discussed in Section III-A (in particular points 2 and 3). The reason is twofold. First, since the W_i's can take any value within a predefined expected interval, the SRT-MTIT is able to catch spatial features of varying extents in the rainfall field. Second, in correspondence of small temporal variations of m, small variations of the reconstructed fields generally are expected.

Both reasons are direct consequences of points 1 and 4 cited in Section III-B, Referring to the utilization of a GOST, in fact, the GOST explores the space of solutions without limiting the search to one single region of attraction of a local minimum, as do deterministic search methods. This also helps to limit the problems of stability mentioned in point 3 of Section III-A. Moreover, through the GOST approach, it is not necessary to introduce the additional constraints needed for the convergence of the ART-MTIT [the first term in the right hand side of (7)] in the error functional. Thus, a simply adapted version of the classical MSE is used for SRT-MTIT, namely

$$E(k, \hat{k}(a), N_p) = \sqrt{\frac{\sum_{j=1}^{N_p}(k_j - \hat{k}_j)^2}{N_p} \Big/ \frac{\sum_{j=1}^{N_p} k_j}{N_p}} \quad (13)$$

where $k = [k_1, k_2, \cdots, k_{Np}]$ is the vector of the observed mean-specific attenuations along the measurement paths. Its jth element is

$$k_j = m_j/l_j, \qquad j = 1, 2 \cdots N_p \quad (14)$$

where l_j is the length (in km) of the jth path. $\hat{k}$ is analogously related to $\hat{m}$.

To introduce the SRT strategy, we start from a basic problem brought about by the new reconstruction model. How can one

estimate the minimum number of PC's that best fit $\boldsymbol{m}$? Given the rainfall field, the network topology, and the set of search parameters (viz., a threshold value for E), estimating N_{PC} is not a straightforward task. An analysis of the covariance matrix of $\boldsymbol{m}$, accounting for topological correlations, cannot lead to more than a rough estimate. Furthermore, even if N_{PC} could be estimated *a priori*, the dimension of the space of solutions would be as large as $N_{\mathrm{PC}} \times 4$. An already difficult direct search in such a large space would be further complicated by the very high degree of multimodality of the error functional E, due to underconditioning. This is always true under the hypothesis (consistent with practice and understood in this paper) that the microwave monitoring network does not operate a regular and dense sampling of the region. Therefore, the search for the absolute minimum of E turns out to be an ambiguous problem in most cases and is strictly related to the problem of determining N_{PC}.

The observations above have two important consequences for the SRT strategy.

1) N_{PC} is not fixed *a priori*. It is a maximum accepted value compatible with the network resolution. The core of the SRT is a tree search strategy that determines the minimum number of PC's needed to reconstruct the observed rain field while meeting the imposed requirement on the threshold of E.

2) Given the basic ambiguity of the information carried by $\boldsymbol{m}$ and the nonorthogonality of the basis functions (see point 3 in Section III-B), it is assumed that the search for one, single, optimum solution does not guarantee its reliability. Instead, it is considered effective to find a set of different and acceptable solutions, each adequately fitting $\boldsymbol{m}$, to be checked later and possibly discarded or modified (SRT was experienced typically to produce a number of solutions ranging from one to ten). The acceptability of a single solution is checked simply by comparing the related value of E with a fixed threshold E_{TF}.

2) Initial Generation Phase of the SRT: The PSS Module: The SRT carries out first a nonexhaustive and extremely simplified initial search that intrinsically solves the aforementioned problem of determining N_{PC}. The search algorithm, referred to as PSS, is the core of the whole SRT, sketched in Fig. 4. The modules RSS, RSO, and MAS carry out different functions of the optimization phase that follows the PSS. For the reader's convenience, we outline each module of Fig. 4 (in particular the PSS introduced here), while the detailed description can be found in Appendix.

The PSS module first processes the observed attenuation vector $\boldsymbol{m}$ and extracts a number of PC's out of A4. These PC's become the first stage nodes of a search tree. The algorithm applied to extract the PC's is a modified version of the Timmer algorithm (referred to as ATA1) [16], [17]. ATA1 randomly and uniformly samples the E function over the search domain A^4. The attenuation vector $\hat{\boldsymbol{m}}$ generated by each PC found by ATA1 must meet the following two requirements:

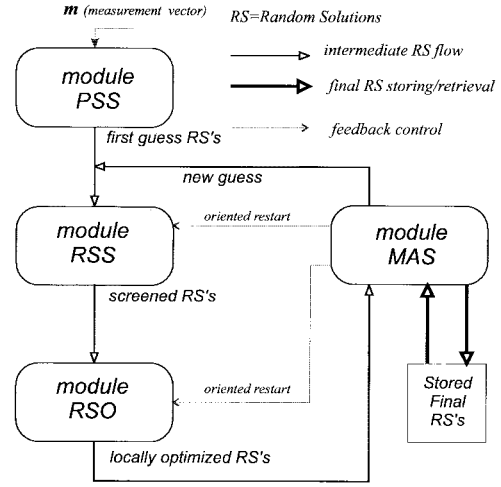1) It must bring the corresponding error functional, defined as in (13), below a fixed threshold E_T.

Fig. 4. Global scheme of the SRT algorithm.

2) Each component of $\hat{\boldsymbol{m}}$ must not exceed the corresponding component of the observed attenuation vector $\boldsymbol{m}$.

The search tree proliferates from these PC's (nodes) by applying the algorithm described by the flow diagram of Fig. 5. The residual attenuation vector is computed by subtracting the attenuation vector from $\boldsymbol{m}$, contributed by the corresponding PC. The residual vector then is assumed as the updated version of $\boldsymbol{m}$, and processing continues in the same way. The reason for condition 2 is that the positive contribution to $\hat{\boldsymbol{m}}$ by each new PC (node) is added to that of parent PC's previously generated in the same branch. Therefore, an overestimate would produce an unrecoverable error in E in the lower branch nodes. Only in those cases in which ATA1 is unable to find any solution is the constraint 2 relaxed (namely, a second version of the Timmer algorithm, referred to as ATA2 is used). When this occurs, proliferation at that node is stopped, regardless of whether $E < E_{\mathrm{TF}}$ or not. Notice from Fig. 5 that this is one of the three conditions in correspondence of which, proliferation of a branch is stopped. In such cases, an RS is found. An RS is a candidate solution, made by the current PC and its parent PC's in the corresponding branch, that can be kept (and optimized) or discarded. The three stopping conditions are the following.

Stop 1: E becomes smaller than a fixed threshold E_{TF}. The RS is kept.

Stop 2: *Stop 1* has not occurred, but the maximum allowed N_{PC} is reached. The RS is discarded.

Stop 3: Neither *Stop 1* nor *Stop 2* has occurred, but the residual attenuation vector has one or more negative components (this can occur only after using ATA2 as a consequence of the fact that ATA1 was not able to find any PC giving $E < E_T$). The RS is discarded.

3) Iterative Optimization Phase of the SRT: The set of RS's generated by the PSS module is the result of a random, preliminary screening of the search space. For this reason, the SRT starts an optimization phase loop (see Fig. 4) on the initial or intermediate set of RS's, with the following basic objectives:
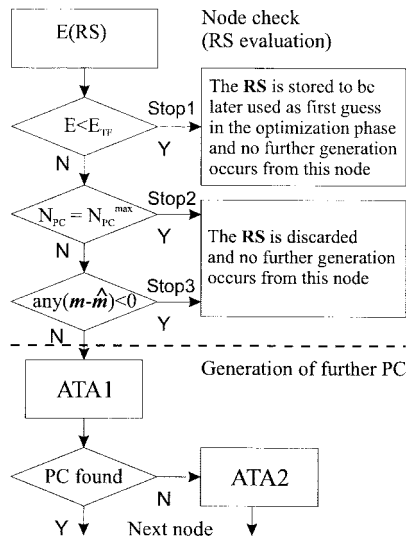
Fig. 5.   Flow diagram of the operations performed on the (residual) attenuation vector at each node of the PSS search tree.

1) Eliminate certain kinds of anomalies that the initial search or the following refinements may have introduced in the set of current RS's;
2) Search for local minima of the error functional, starting from the current set of RS's;
3) Apply certain criteria to check the consistency of the refined RS's and consequently decide whether the refinement process should be stopped or a new iteration should be started.

Detecting and removing anomalies is an essential task, since PSS performs a somewhat "blind" search. The typical problem encountered is that two or more RS's are made up by almost identical PC's but with a different sequential order. Therefore, the PSS assumes that they correspond to different rainfields. In addition, two opposite anomalies may occur. The first occurs when an RS includes two similar PC's that easily can be merged together without modifying the estimated field. The second occurs when an RS includes one or more PC's that can be eliminated, since their distance from all microwave links is such that they give no significant contribution to any of them.

In particular, the task of the RSS module is to check and organize routinely the initial or intermediate RS's, accounting primarily for their physical consistency. Notice that the elimination or mitigation of the aforementioned problems, as performed by the RSS, is of paramount importance both for computational time and stability of the whole SRT, as discussed in the Appendix. One obvious reason is that, once the RS's have been refined by removing or limiting the aforementioned anomalies, the RSO module utilizes them as first guesses to start the search for the local minima of the error functional E. In other terms, the RSO module explores $A^{\text{NPC}\times 4}$ very closely to the current RS's and adjusts them slightly with the purpose of reducing E.

All operations made by the RSS and RSO modules are controlled by the MAS module, which basically performs a statistical analysis on the set of current and previous RS's. The purpose is to verify whether or not a significant reduction

of the error functional is likely (which would necessitate the continuation of the optimization phase through further iterations by RSS and RSO). In the latter case, the optimization loop is stopped, and the current set of RS's is taken as one final SRT solution.

IV. DYNAMIC RECONSTRUCTION OF RAINFALL FIELDS

The previous sections were devoted to the problem of reconstructing static rainfall fields. Here, we analyze the issue of their continuous reconstruction (over a time interval of several minutes), accounting for the dynamic evolution of the observed rainfall fields. The DRT is based on the SRT, properly modified for dynamic reconstruction. A "sampling" period of 1 min is assumed for the microwave monitoring system. This is small enough to fit into observed dynamics of measurements when rainfall events develop rapidly. It is opportune (in particular for hydrological applications) to perform *a posteriori* evaluations on reconstructions averaged over longer time intervals (e.g., at least 15 min).

A. Basic Principle of the DRT

Efficient exploitation of the SRT-MTIT asks for a correct analysis of its random outputs (reconstructions). In this regard, it is actually impossible to define a general method of statistical analysis that, applied to the set of solutions at a given instant, efficiently identifies reliable and unreliable sets of solutions. In [18], through an in-depth analysis of the SRT-MTIT outputs, we pointed out some statistical features that help to detect those outputs that can be considered unreliable. These are 1) a spread of more than 20% of the mean rainfall estimate of the different solutions and 2) the simultaneous presence of some solutions made by a small number of PC's [e.g., 3)] and of some others made by a large number of PC's [e.g., (3), (7)]. In the same paper, we demonstrated that the reliability of the SRT static reconstructions cannot be easily inferred if they are not analyzed in their temporal sequences. Furthermore, it was noted that a "critical" placement of rain cells with respect to the monitoring network sometimes makes the static reconstruction unreliable.

It was mainly for the reason mentioned previously that the DRT was developed. The objective was to efficiently exploit the temporal correlation of consecutive measurements in order to increase the reliability of the reconstruction over a more extended temporal window. The DRT exploits the small variations observed between subsequent m vector samples, detected by means of a threshold applied to the correlation between two consecutive m vectors.

As mentioned in Section III-A, there was no evidence of systematic correlation between two consecutive reconstructions by ART-MTIT, and neither was there any in some cases when the differences among the associated attenuation measurements were small. When imposing the ART-MTIT solution reached at the preceding time step as an initial condition for iterations at the current time step, we obtained a rapid degradation of accuracy at the third step in 58% of cases on average. On the other hand, reasonably, it can be expected that two successive SRT solutions would be

made up of the same PC's, slightly changed in their original positions, widths, and heights. This follows from the fact that the nonorthogonality and the continuity of the SRT basis functions set significantly mitigate the problems of stability (whether they are due to small variations of measurements or to uncertainties in them) that occur when a rigid basis functions set is adopted, as in ART.

The DRT is based on the aforementioned SRT feature. At the first time step, the rainfall field is reconstructed through the full SRT, while the following reconstructions are obtained by applying only its iterative optimization phase. In other words, the solution at the following time steps is obtained by further processing the initial solution provided by the PSS module at the first time step. Actually, the SRT is modified as follows in the new DRT context.

1) The current vector $\boldsymbol{m}$ is compensated for the difference between $\hat{\boldsymbol{m}}$ and $\boldsymbol{m}$ at the previous time step.
2) The small perturbation hypothesis is checked on the current compensated $\boldsymbol{m}$, compared to the previous one.

B. Predictive Function of the DRT

Aside from exploiting the SRT correlation properties, the DRT also takes advantage of information brought by the temporal evolution of the event. In fact, the DRT basic principle discussed previously is related strictly to that used in the RSO module, described in detail in Section I-C of the Appendix. The local search is made in a bounded area around the solution found at the preceding time step. Also, we found that performance was improved by choosing the bounded local search domain through a prediction based on a statistical analysis of the evolution of the PC's. This was made as follows. After the first reconstruction, the "perturbation" array $\boldsymbol{p}^{(m)}$ at the mth time step was considered, defined as

$$\boldsymbol{p}^{(m)} = \boldsymbol{a}^{(m)} - \boldsymbol{a}^{(m-1)} \tag{15}$$

where $\boldsymbol{a}^{(m)}$ and $\boldsymbol{a}^{(m-1)}$ are the solutions at time steps m and $m-1$, respectively. Considering a temporal window of M time steps preceding the current step m, let us define the 2-D array σ whose generic component σ_{ij} is

$$\sigma_{ij} = \frac{\sqrt{\sum_{n=m-M+1}^{m} (p_{ij}^{(n)} - \overline{p}_{ij})^2}}{M-1} \tag{16}$$

where

$$\overline{p}_{ij} = \frac{\sum_{n=m-M+1}^{m} p_{ij}^{(n)}}{M}. \tag{17}$$

Therefore, $\overline{p}_{ij}$ and σ_{ij} are, respectively, the mean and standard deviation estimates of the perturbation of a_{ij} evaluated over the M steps interval. Such parameters are used to define the domain boundaries for the local search at the following time step. To go into detail, in (A2), the position functional $B(\boldsymbol{a})$ of (A3) is substituted for with the dynamic position functional defined as follows:

$$\begin{aligned} B_{\text{dyn}}(\boldsymbol{a}) = 1 + \sum_{i=1}^{N_{\text{PC}}} \sum_{j=1}^{4} (&\exp[-w_{ij}\sigma_{ij}^{-1}(\widehat{a}_{ij}(\sigma_{ij}) \\ &- a_{ij} + p_{ij})] \\ &+ \exp[-w_{ij}\sigma_{ij}^{-1}(a_{ij} - \breve{a}_{ij}(\sigma_{ij}) - p_{ij})]) \end{aligned} \tag{18}$$

where $\widehat{a}_{ij}$ and $\breve{a}_{ij}$ are indicated explicitly as functions of σ_{ij}. Hence, large values of the σ components relax the bounded local search. On the other hand, small values force the algorithm to search for the next solution in a well-defined local domain.

The E_b value thus obtained is then checked. Should DRT not be able to reduce E_b below E_{TF}, then the new attenuation data must be processed again through the full SRT.

We point out that a major feature of this technique is its speed. It requires approximately 20% of the full SRT average processing time. Hence, it is possible to perform more complex and time-extended investigations in real time in order to exploit temporal correlation. Such investigations have shown that the choice of the initial $\boldsymbol{a}$ vector is a key point for the DRT performance. Recall that, in fact, the SRT provides a whole set of $\boldsymbol{a}$ vectors. While two solutions never differ by more than 30% from each other in terms of average rainfall rate, important differences in PCs' positions can be found. This problem has been faced observing that, given a good initial reconstruction, the DRT is able to track the same event for a longer time. So a parameter of reliability of the initial solution (and therefore of the whole tracking that follows) is simply the number of consecutive reconstructions that the DRT has been able to obtain.

V. SIMULATIONS AND RESULTS

A. Simulations and Evaluation Parameters

The results shown and discussed in this section were obtained through simulations, as in [5]. However, a major difference with respect to that paper is that the rainfall fields utilized here as "ground truth" have not been simulated through a rainfall model, but derived from reflectivity data collected by the weather radar station installed in Montagnana (Firenze) [6] and converted to rainfall rate through a standard reflectivity–rainfall relationship. Reflectivity data are those of a rainfall event occurring in central Tuscany on November 10, 1994 and monitored by the weather radar with a range resolution of about 125 m, an azimuth resolution of about 1°, and an antenna rotation period of about 1 min. The elevation angle is less than 2°. The whole radar observation lasted 30 min. The selected area lies between 20 and 50 km from the radar station, within a clutter-free zone. Radar data then have been resampled on a 250 m square grid. Since the intrinsic resolution of radar-derived rainfall fields is higher than that of the microwave network, such fields can be taken as ground truth with good approximation.

Though the considered rainfall event was not particularly intense, it is quite interesting for our purposes because of its fast evolution (see Fig. 6). Basically, it consists of two
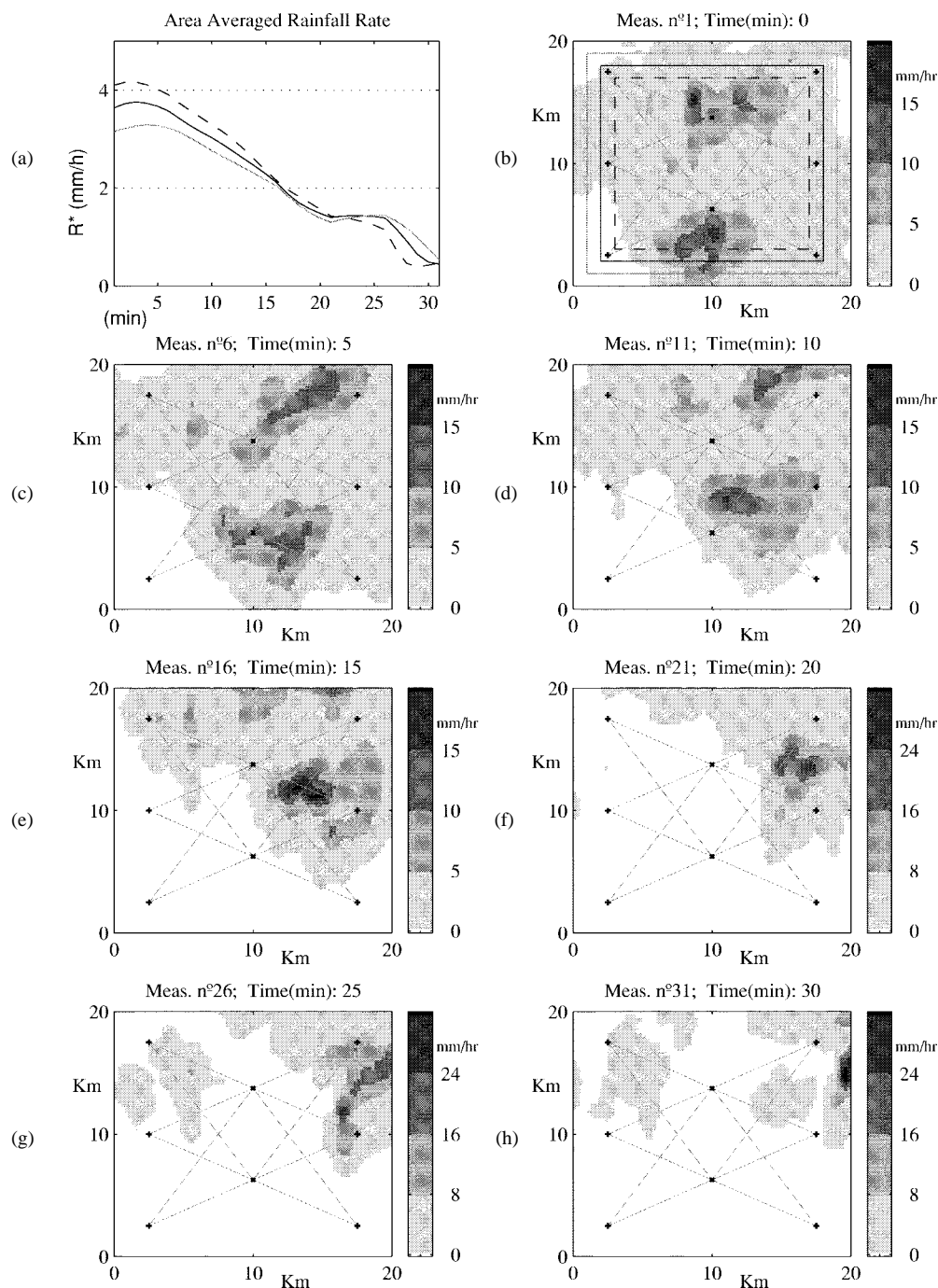
Fig. 6. (a) Spatially averaged rainfall rates from the beginning of monitoring. The line styles correspond to the style of the rectangles in Fig. 6(b), evidencing the three different areas where the averages are evaluated $(A'_R, A_R,$ and $A''_R)$. (b)–(h) Rainfall field snapshots taken every 5 min [note that the gray scale assignment to rainfall rates changes from (f) to (h)].

main rain cells moving from the southern to the northeastern zone of the monitored area and of a third small cell coming closer to the northwestern zone in the last 10 min of the event. In Fig. 6(b), the *a posteriori* evaluation area A_R is evidenced by the continuous black contour. All statistics and error functionals were computed over that area. The other two areas A'_R and A''_R within the dashed and gray rectangles were shown with only one purpose in mind: to point out, through the average rainfall rates plotted in Fig. 6(a), the aforementioned

critical conditions of the final phase of the observation (the cell giving maximum contribution to the average rainfall rate lies on the edge of the monitored area).

It is worthwhile to focus on the following aspects, which are highly relevant to the evaluation of results.

Accuracy in the estimation of the mean rainfall rate over the area: The results that are reported in this paper (and that were obtained in general) show that both ART-MTIT and SRT-MTIT perform well in terms of the normalized bias of the

mean rainfall rate estimate over the monitored area, namely

$$\text{NBIAS} = \frac{\text{BIAS}}{\overline{R(x,y)}} \qquad (19)$$

with

$$\text{BIAS} = \overline{\hat{R}(x,y)} - \overline{R(x,y)} \qquad (20)$$

where

$$\overline{f(x,y)} = \frac{1}{A_R} \iint\limits_{A_R} f(x,y) \, dx \, dy. \qquad (21)$$

General performance of the monitoring system: To evaluate it, we utilized two *a posteriori* evaluation parameters. They are useful to compare ART-MTIT and SRT-MTIT, quantifying their capability to reproduce the basic features of the rainfall fields. The first is the classical normalized MSE, with bias removed

$$\text{NMSE} = \frac{\sqrt{\overline{\left(\hat{R}(x,y) - R(x,y) - \text{BIAS}\right)^2}}}{\overline{R(x,y)}}. \qquad (22)$$

The main drawback of NMSE is that it is not able to bring out the higher spatial frequencies of the local error. Therefore, it cannot be exploited to check whether a reconstruction is "smoothed" (i.e., whether the original major features, through which rain cells can be identified, have been strongly smoothed by the reconstuction algorithm). A different parameter, used in the statistical analysis of precipitation and overcoming such inconvenience, is that proposed by Rousseau [19]. In this paper, an extended version is applied to analyze the reconstructed fields. Given a rainfall intensity discrimination threshold t (we alternatively use the normalized rainfall discrimination threshold t^o, namely t normalized to the maximum rainfall rate of the true rainfall field), the areas of the true and of the reconstructed rainfall fields, where the rainfall rate is greater or smaller than t, are identified. These are used in the following formula:

$$I_R^t = \frac{4p_{11}p_{00} - (p_{10} + p_{01})^2}{(2p_{11} + p_{10} + p_{01})(2p_{00} + p_{10} + p_{01})} \qquad (23)$$

where

$$p_{ij} = \frac{1}{A_R} \iint\limits_{A_R} T_{ij}^{(t)}(R(x,y), \hat{R}(x,y)) \, dx \, dy \qquad (24)$$

and

$$T_{ij}^{(t)}(\xi, \xi') = \begin{cases} 1, & \text{for } \begin{cases} (2i-1)\xi > (2i-1)t \\ (2j-1)\xi' > (2j-1)t \end{cases} \\ 0, & \text{elsewhere} \end{cases} \qquad (25)$$

and A_R is the area where the rainfall field reconstruction is made. Thus, p_{11} is the percentage of A_R at which rainfall rate exceeds the threshold t, both in the true and reconstructed field. p_{01} is the percentage of A_R at which rainfall rate is smaller than t in the true field and exceeds t in the reconstructed one. p_{10} and p_{00} are defined analogously. For a given t, p_{11} and p_{00} can be considered alternatively as the probability that the local rainfall rate is correctly placed by the reconstruction algorithm above or below such threshold,

and p_{01} and p_{10} as probabilities of wrong placement. I_R^t may range from -1 (completely wrong reconstruction) to 1 (perfect reconstruction). As a rule of thumb, we can say that to achieve $I_R^t = 0.6$, the reconstructed field must not miss more than 20% of local values ($p_{01} + p_{10} \leq 0.2$). The ability of such a parameter to evaluate the reconstructions is well evidenced by Fig. 7. The four gray levels used in the three rainfall maps (the original and the two reconstructions) also are shown in the I_R plot for the reader's convenience. The value of I_R depends on the similarity between the reconstructed and the true field, in terms of shape and position of the isohyets corresponding to a given value of the threshold. For instance, notice that in the $3 \div 6$ mm/h band, the ART reconstruction is closer to the true field than the SRT reconstruction, and the corresponding I_R values are accordingly slightly higher, while the opposite occurs from 6 to 12 mm/h.

With regard to reconstruction speed, to obtain a single reconstruction through the ART-MTIT or a complete set of reconstructions through the SRT-MTIT, a few tenths of seconds are needed with a common 100 MHz Pentium personal computer. In the SRT-MTIT case, a maximum limit of some minutes was reached when search parameters that were not consistent with the network topology were adopted. This may occur, for instance, when a minimum PC width, too small with respect to the spatial resolution of the network, is fixed. In these conditions, the search tree of the PSS module proliferates excessively, and processing time grows exponentially.

B. Discussion of Results

1) ART and SRT: Fig. 8(a) shows the time averaged mean rainfall rate, with particular attention paid to the rainfall rate over the monitored area averaged both in space and time (from the beginning of monitoring (min. 0) to the current time). Fig. 8(b) and (c) shows the corresponding NMSE and NBIAS. The anomalous increase of NMSE occurring approximately 25 min later, is due primarily to the previously mentioned critical position of the rain cells. Fig. 8(d) shows the histogram of NBIAS, computed separately for every reconstruction (without time averaging). Notice that for most instantaneous reconstruction, the absolute value of NBIAS is smaller than 10%. Hence, good accuracy is achieved in terms of mean areal rainfall rate.

The ART-MTIT, though performing well in terms of minimization of NBIAS, is able to reproduce only a very smoothed version of the original rainfall field. This was already evidenced by all values taken by I_R^t that corresponded to high values of the threshold t (e.g., $t^o = 0.6 - 0.75$) in Fig. 7(d), and Fig. 9 further confirms such observation. Fig. 9 summarizes the reconstruction performance over the 30 min observation. Notice in particular the curves of the average values of I_r^t (bold black and gray curves). Evidently, while the ART reconstructions rapidly degrade when $t^o > 0.3$, the SRT reconstructions are satisfactorily accurate up to $t^o = 0.55$. The gray shaded and the dashed areas in the same figure include the 80% (around the median) of the ART and SRT results, respectively. Observing such areas, the above conclusions about accuracy can be extended to the whole population of ART and SRT solutions. Also, notice that in the majority
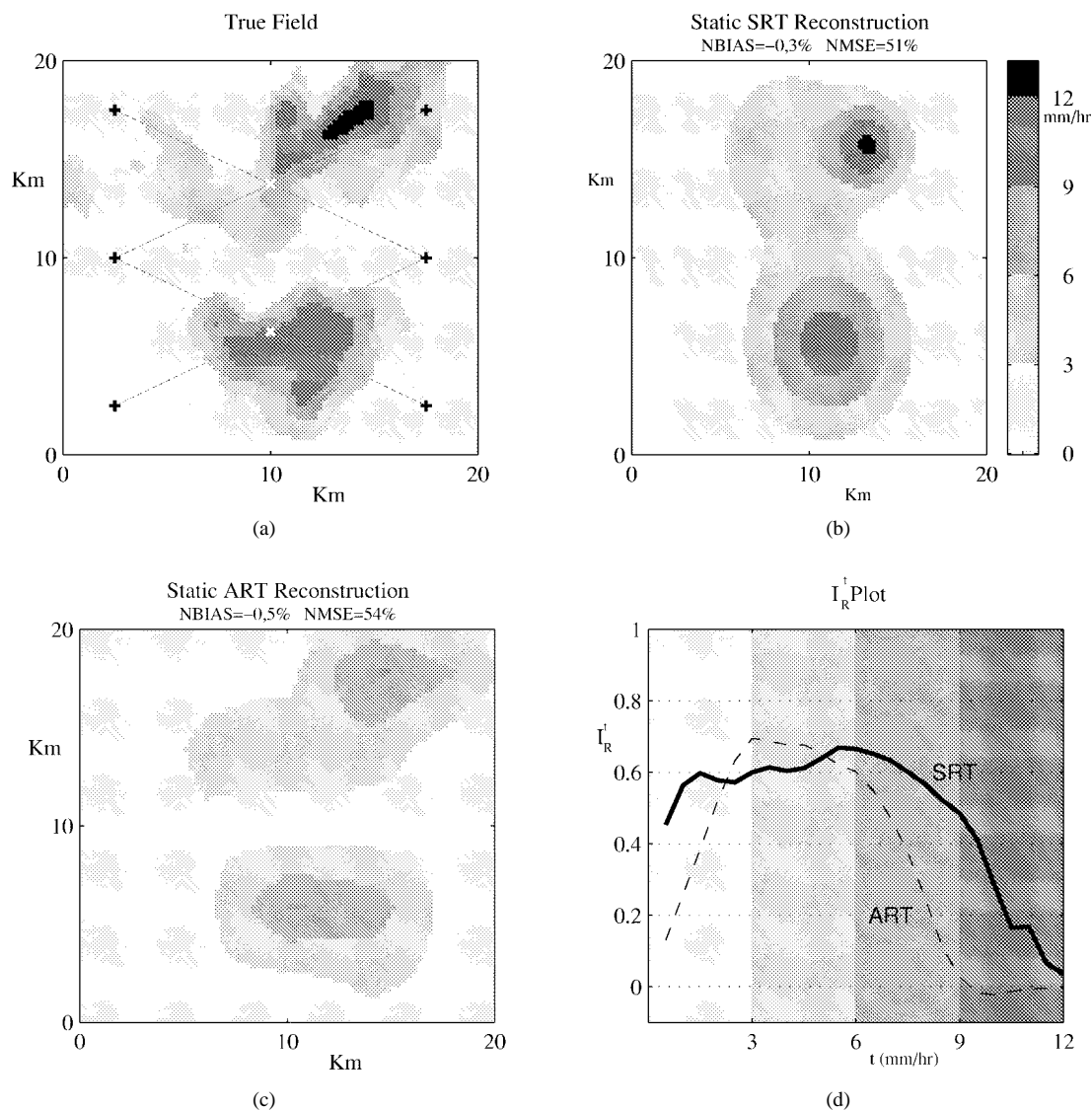
Fig. 7. Example of static reconstruction. (a) True rainfall field. (b) SRT reconstructed rainfall field. (c) ART reconstructed rainfall field. (d) I_R^k plot, with k ranging from the minimum to the maximum rainfall rate in the evaluation area A_R shown in Fig. 6. The continuous line refers to (b), and the dashed line refers to (c). Both are compared to (a).

of cases, neither the SRT nor the ART succeed in correctly locating and estimating the maxima of rainfall rate (see the curves approaching zero for high values of the threshold t. This undesired feature is more pronounced in the ART case.

The rainfall rate maps shown in Fig. 10 are averaged over the whole 30-min interval, and the true field in the upper left can be compared with the five reconstructions reported. Two of them are obtained with a higher resolution network (NET2). For the moment, disregard Fig. 10(b), which is relevant to the DRT and discussed in the next section. Comparing the reconstructions in Fig. 10(c) and (d) with those of Fig. 10(e) and (f), notice the generally improved performance of NET2. Notice also, in the ART reconstructions, some of the aforementioned effects of the rigidity of the basis functions grid. In particular, there are some features that would be difficult to interpret, such as that in the upper left of Fig. 10(d) and the cell missed [also in the upper left corner, Fig. 10(f)].

It can be concluded therefore, that the SRT-MTIT exhibits greater ability in identifying the single rain cells contributing to the total field and in correctly estimating the center cell intensities and widths. The residual uncertainty depends mainly on the position of the rain cell with respect to the monitoring network. Trivially, the higher the network spatial resolution, the smaller the expected error made when positioning the PC [see Fig. 10(c) and (e)].

2) DRT Compared to ART and SRT: Let us now consider Fig. 10(b), showing the DRT reconstruction after 30 min, and Fig. 11 (analogous to Fig. 9), plotting I_R values for the whole 30 min observation. The prediction, based on previous reconstructions, implicitly allows the DRT to extend the area outside the monitored zone, where reconstructions can be considered reliable. In fact, compare the reconstructed fields of Fig. 10(b)–(d), and notice that both the SRT and ART tend to project into the monitored area even the contributions of cells that lie just outside, while the DRT mitigates this effect. In
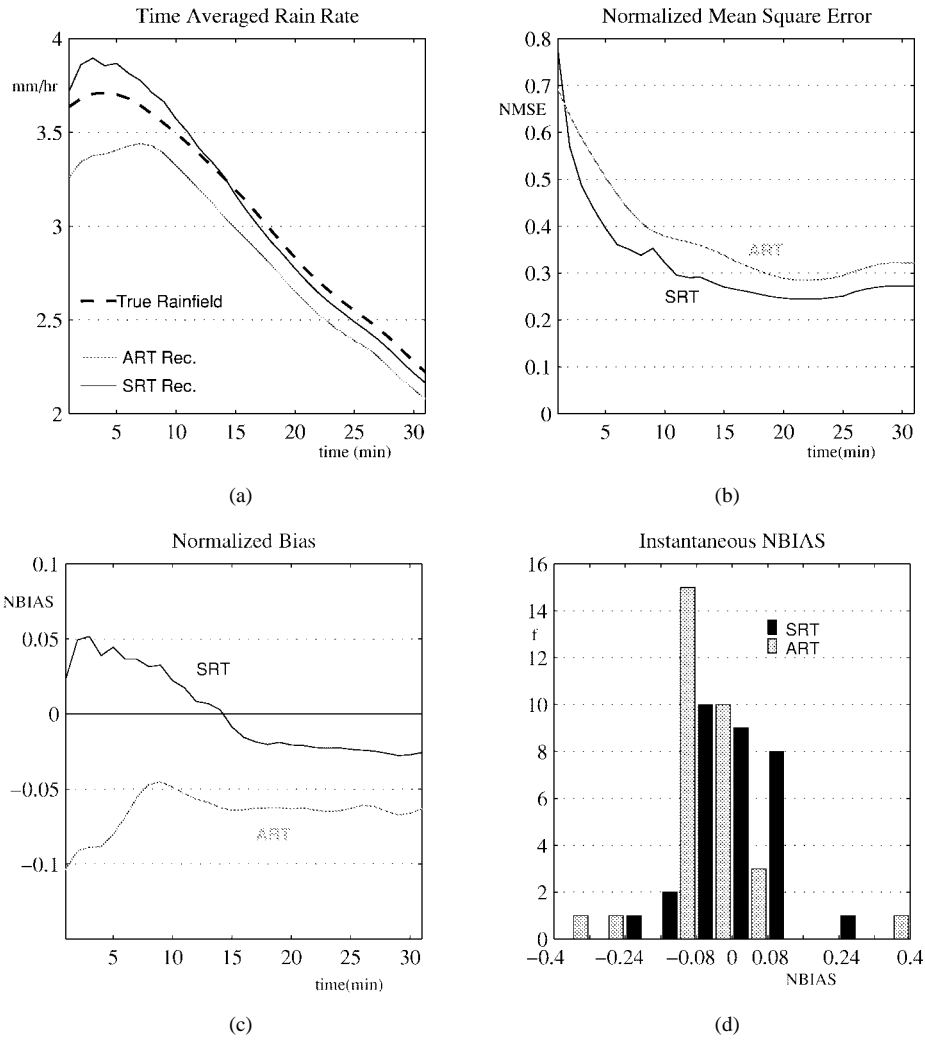
Fig. 8. Summary of statistics of static reconstructions. All gray lines refer to ART reconstruction and all continuous black lines refer to SRT reconstruction. (a) Mean rain rates averaged in time: true (dashed), SRT reconstruction (black), and ART reconstruction (gray). (b) Cumulated NMSE. (c) Cumulated NBIAS. (d) Histogram of the instantaneous NBIAS.

this regard, observe the large cells in the northeastern corner of Fig. 10(b). These are reconstructed with quite acceptable approximation, even if there is no measurement path crossing them. This success is derived from the DRT's ability to solve the ambiguity of data measured in the critical phase (the last 10 min) by exploiting the much more reliable set of PC's obtained at min 21 by the SRT and then adopted as initial conditions for the following reconstructions. An *a posteriori* evaluation carried out separately confirmed that the last reliable SRT reconstruction is that of the 21st min. After that, the static reconstructions often were unable to place the PC's correctly. This also is evident from the aforementioned sudden increase of NMSE in Fig. 8(b).

Fig. 12 demonstrates the critical importance of reconstructing the event in the last monitoring minutes. The left hand plots show I_R^t of the whole sequence of instantaneous reconstructions by ART, SRT, and DRT for three different discrimination thresholds. Instead, the right-hand plots show I_R^t relevant to time-averaged reconstructions, primarily obtained by averaging all the reconstructions from the beginning to the current instant. The zero values taken by I_R^t in the final minutes are

due to the aforementioned critical position of rain cells outside the monitored area. Notice that the SRT loses the ability to reconstruct the correct position and intensity of rainfall cells sooner than the DRT (and this is far more evident when high thresholds are considered). The left-hand plots are indicative of the peculiar ability of the DRT to continuously track the major features of the precipitation. In fact, the SRT performance (in terms of I_R^t) rapidly decreases when increasing the threshold. For $t^\circ = 0.75$, the pronounced temporal fluctuations of I_R^t denote a general degradation of estimate accuracy of the cells' intensities.

The substitution of the global search performed by the SRT, with the local search performed by the DRT, can enhance the effects of BIAS and NMSE obtained in the initial reconstruction, with the effect being to increase the cumulated NBIAS and NMSE. For this reason, the DRT solutions need to be checked after a maximum tracking interval, by comparing them with one or more SRT results. For instance, in the event considered, the DRT utilizes the SRT at min 1 for initial setup and then at min's 12 and 21, since it does not succeed in reducing E_b below E_{TF}. Fig. 12(c) shows that the I_R^t and
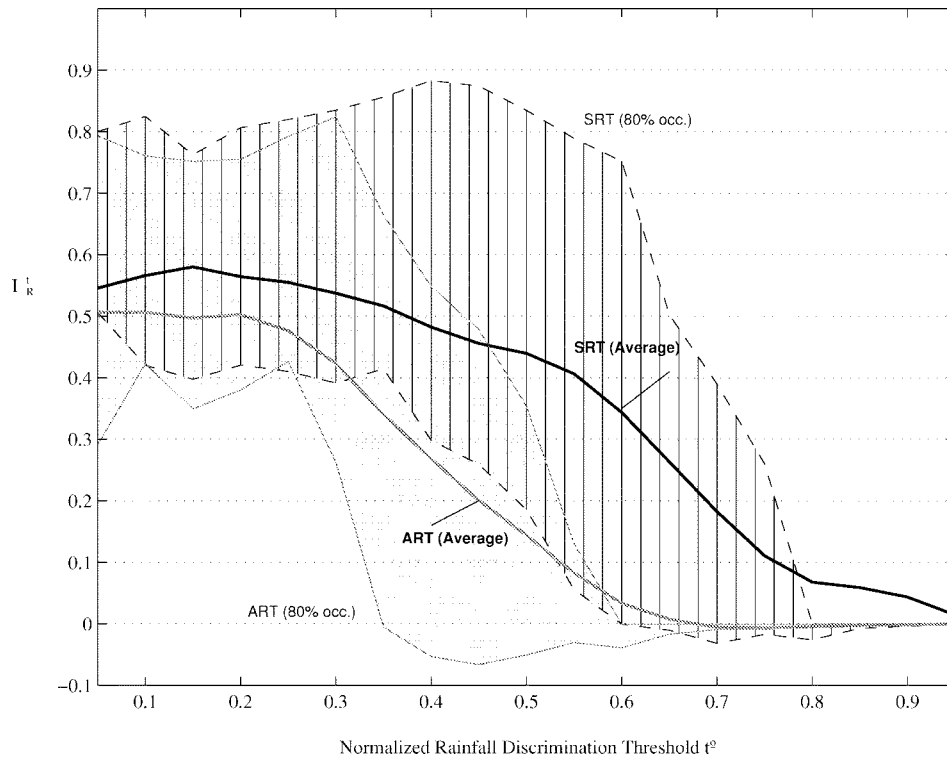
Fig. 9. I_R^t dispersion plots at the 30th min. Bold gray line: ART reconstructions, black line: SRT reconstructions. Gray and dashed areas refer to the dispersion interval of ART and SRT reconstructions, respectively, including the 80% of results (around the median).

$t = 0.75R_{\max}$ fall to zero at min 10, thereby exhibiting a delay of at least one reconstruction before deciding to use the full SRT again.

After each full SRT application, all solutions are employed as initial conditions by the DRT. For the reasons mentioned in Section IV-B, the analysis of the evolution of each solution, based on the DRT predictive function, is decisive. In fact, the longer a solution is able to generate reconstructions at the following time steps (through slight adjustments of the prediction), the higher is its probability to be a reliable solution (and the same obviously holds for all the subsequent reconstructions). For this reason, the DRT reconstructions are more reliable than static reconstructions. The time-extended analysis selects the most adequate SRT solutions.

As a final remark, we envisage that a combined application of SRT and DRT in the postprocessing of measured data could be even more effective. The statistical analysis of SRT outputs then should be extended in time, providing more accurate indications about the reliability of reconstruction. This would allow one to single out those static solutions that are optimal, to apply the DRT both in forward and backward mode.

3) Measurement Errors and Their Effects on the DRT: Three kinds of measurement errors are relevant to the tomographic system considered.

Errors affecting each measurement path independently from the others: Among these are system antennas misalignments, anomalous propagation, and local variations of the parameters of the k–R relationship. These errors can be modeled through a highly uncorrelated zero-mean noise vector added to the measurement vector $\boldsymbol{m}$. Obviously, when it causes negative attenuation measurements, the corresponding

$\boldsymbol{m}$ components are set to zero. The main effect is to shorten the sequences of dynamic reconstructions (i.e., the full SRT is applied more frequently). In fact, the correlation of subsequent measurements is reduced by these kinds of errors. Therefore, the predictive function of the DRT is inhibited more frequently.

Errors affecting all measurement paths with high correlation: These include additional attenuation due to molecular absorption by O_2 and water vapor and large scale bias due to the adopted k–R relationship parameters. Such errors were modeled through an additional random attenuation field $k'(x, y, t)$ with a spatial correlation comparable to the size of the monitored area and a time correlation comparable to the duration of the whole event. Notice that the attenuation measurements are path-averaged, and that this further increases the correlation among the $\boldsymbol{m}$ components.

Errors due to receiver noise: The noise power at the receiver and the transmitted power define the dynamic range of the system. In turn, the dynamic range and the maximum expected rainfall rate define the maximum admissible path length for a given operating frequency. Its effects are negligible, unless "path blinding" occurs. This is when the attenuation brings the received power to a level comparable to that of noise. In this case, the algorithm converges anyway. Obviously, the accuracy of reconstruction deteriorates dramatically as the number of "blinded" paths increases.

Fig. 13 shows the time-averaged NBIAS and NMSE obtained by applying to the DRT sequence considered in Section V-B2 noise of type 1) + 3) and 2) + 3). The two cases are evidenced by dashed and dotted lines, respectively. The continuous lines refer to reconstructions not affected by noise. Each curve represents the average of 50 DRT reconstructions
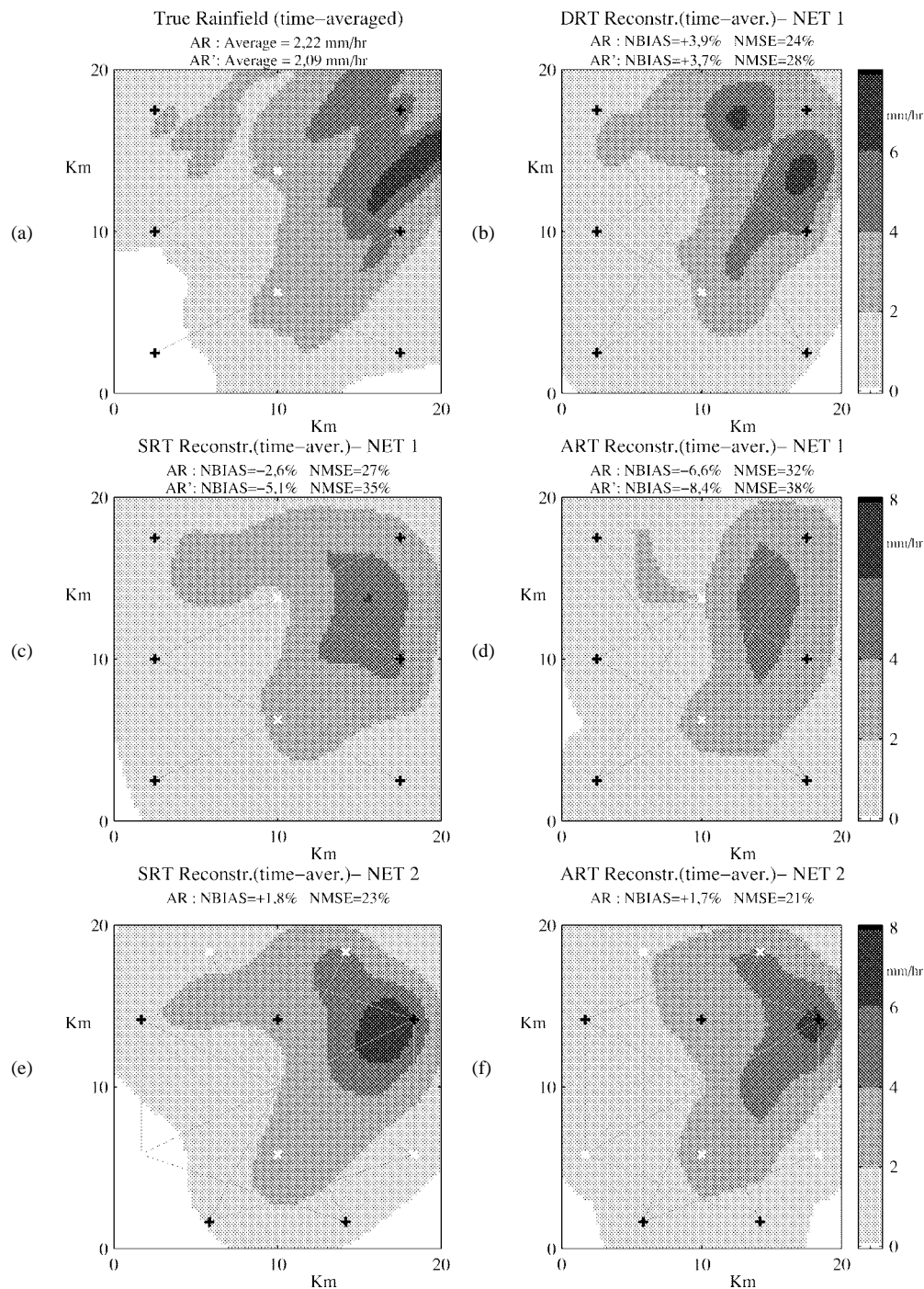
Fig. 10. Summary of reconstructions averaged over the 30 min observation. (a) True time-averaged rainfall field. (b) DRT reconstruction with a low-resolution network (NET 1). (c) SRT reconstruction with NET 1. (d) ART reconstruction with NET 1; (e) and (f) like (c) and (d) but using a high-resolution network (NET 2).

performed on the same sequence of attenuation measurements. Since rainfall was not intense, path blinding never occurred.

Notice that the NMSE curves exhibit a very low sensitivity to noise. While this was expected for the 2) + 3) case, some comments are needed for the 1) + 3) case, for which the SNR at the beginning of the sequence was 10 dB. As mentioned before, the main effect of this noise is that the full SRT is applied more frequently. The SRT, being based on an MSE minimization, pursued by exploiting the spatial correlation

properties of m, is not so sensitive to spatially uncorrelated noise. The two basic drawbacks are that the processing time increases (in the case study it practically doubled), and the short duration of the dynamic reconstructions makes it more difficult to evaluate the reliability of the reconstruction.

As far as NBIAS is concerned, the results of the 2) + 3) case show an increase that is directly proportional to the additional attenuation (an expected value of 0.05 dB/km was assumed for $k'(x, y, t)$ corresponding to an attenuation due to
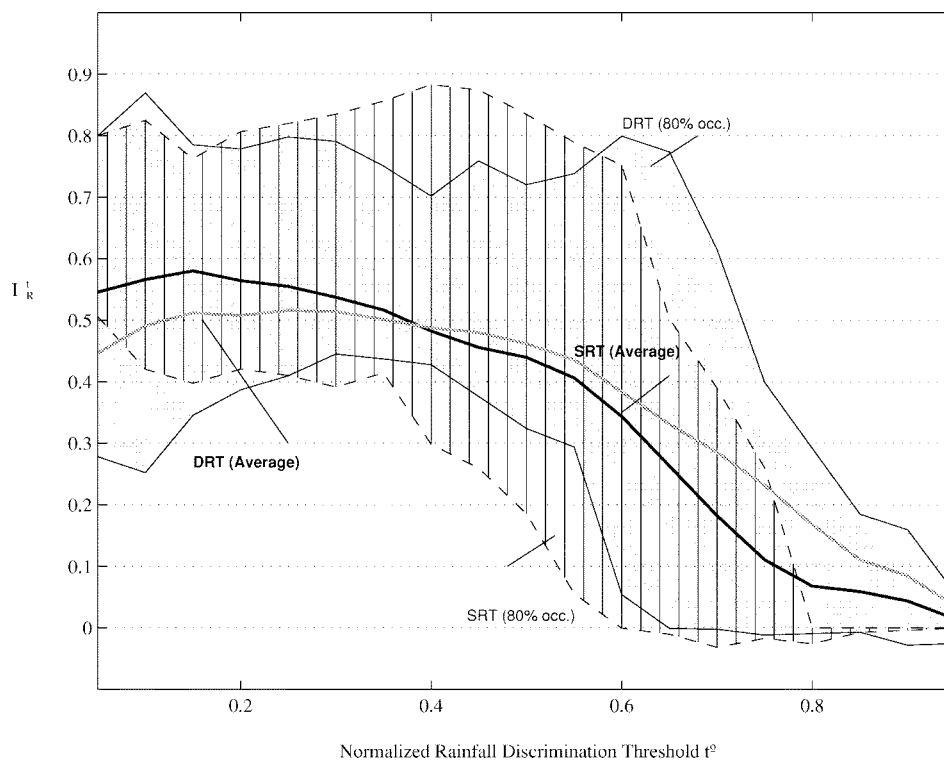
Fig. 11. As Fig. 9, but the gray line and area refer to DRT reconstructions.

approximately 0.25 mm/h rainfall). In the 1) + 3) case, two phases can be distinguished. In the first phase, the plot clearly shows that the zero mean noise does not affect NBIAS. In the second phase on the other hand, a negative attenuation is often detected and therefore directly set to zero. This explains the positive contribution to NBIAS.

VI. CONCLUSIONS

Microwave tomography for rainfall estimation first was proposed in 1991 and is based on attenuation measurements made on a set of independent microwave links, distributed within an area to be monitored. Rainfall fields are estimated as linear combinations of basis functions. The relative simplicity of the solution makes it an alternative (or integrative) solution, with weather radar in areas of limited size and surrounded by complex orography. Furthermore, it originally was shown to be able to provide an improved space-time resolution with respect to raingauge networks at the parity of total number of measurement stations (transmitters and receivers, or rain-gauges). Also, it was pointed out that a microwave tomography system could be exploited profitably not only as a stand-alone system, but also as a reference measurement system at ground in experiments for calibration of radar rainfall estimates or for determining reliable methods to convert radar reflectivity data to rainfall estimates. In fact, the microwave tomography system allows short-time and area-averaged comparisons that low-density raingauge networks are not able to provide. In this perspective, observe that the smoothing action that is intrinsic in the treatment of the attenuation data is a positive factor for the significance of rainfall estimates.

Since that first proposal, which was based on an iterative deterministic approach for ART, it was envisaged that the special inversion problem that must be faced deserved further investigation concerning the optimal choice of the basis functions, the use of adaptive algorithms, and the evaluation of overall system performance with different kinds of precipitation events. In this paper, a more flexible and robust solution to such a problem has been proposed: SRT. This is based on an initial stochastic solution search followed by a finite sequence of optimization and control phases. The new technique always guarantees convergence, even when increasing the number of microwave measurement paths (i.e., the network resolution) at the expense of processing time. However, attenuation data collected by the same high resolution monitoring network easily can be exploited adaptively. Processing time can be traded for spatial resolution by modifying search and optimization parameters (mainly the maximum number of elementary cells used for reconstruction and their minimum extension). This can be made within certain limits, it being useless to increase processing time beyond a threshold related to the maximum achievable resolution. Indeed, a major feature of the new technique is that exploiting the optimization/control modules for a number of time steps exclusively, allows consistent performance and fast, dynamic tracking of DRT, whose reliability can be checked in real time.

Optimization and control modules, as devised, also provide the opportunity to remove anomalies that could not be avoided by the original technique in particular cases. Some examples have been shown in this paper, through simulations based on a rainfall event obtained from real radar observations. This
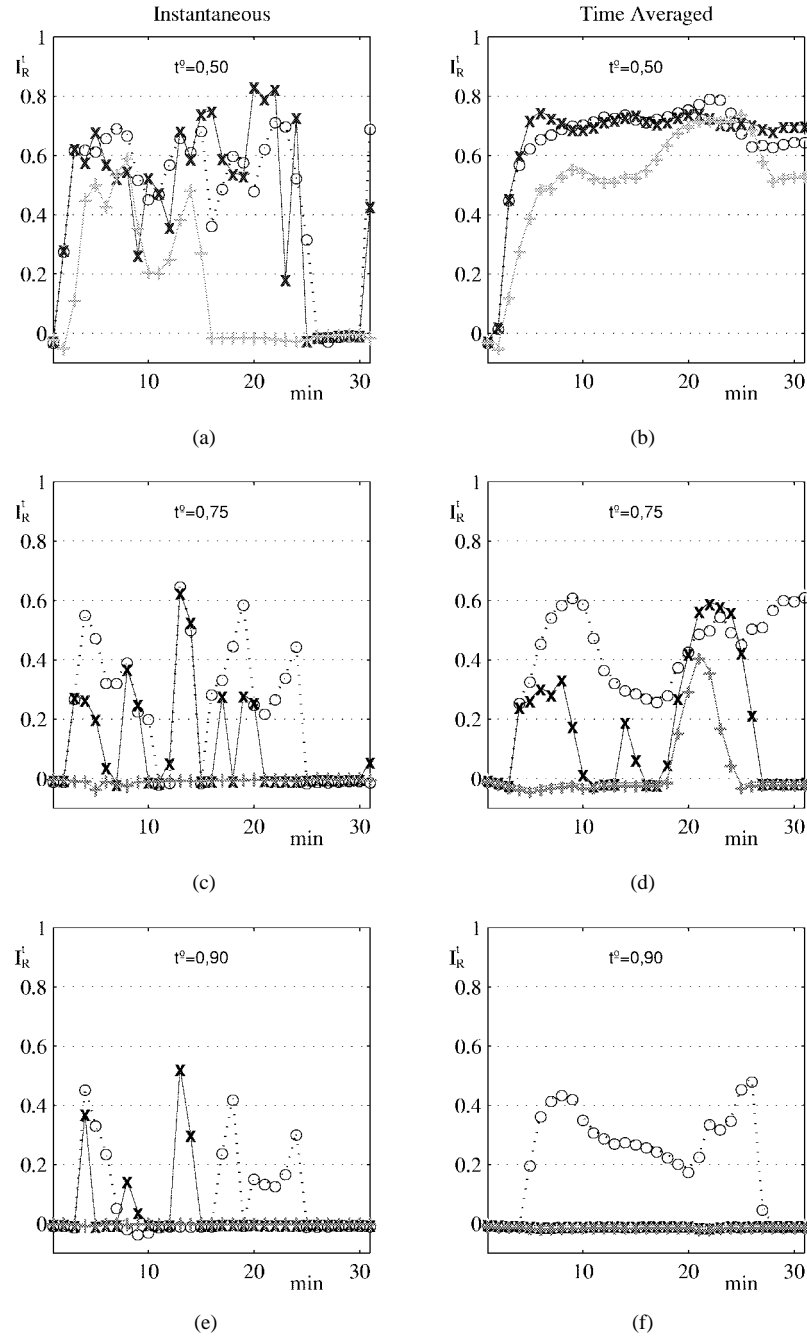
Fig. 12. $I_r^{t^\circ}$ plots versus time for different t° values: DRT (circles on dashed line), SRT (crosses on black line), and ART (crosses on gray line). Left-hand plots: instantaneous reconstructions. Right-hand plots: reconstructed rainfall field averaged in time.

choice guarantees a good adherence of simulations to reality and prevents the shape of the basis functions from influencing the reconstruction performance.

APPENDIX

A. PSS Module and the Adapted Timmer Algorithms (ATA1 and ATA2)

Two different classes of GOST from each node were considered for the PC search in A^4: the simulated annealing methods and the clustering methods [16]. Simulated annealing methods, though relying on a more solid theoretical basis,

could not be adapted easily to the described tomographic problem. Instead, clustering methods combine the advantages of a random sampling of the function domain with a quick convergence of local searches for minima. The general scheme of an algorithm belonging to this class can be summarized as follows.

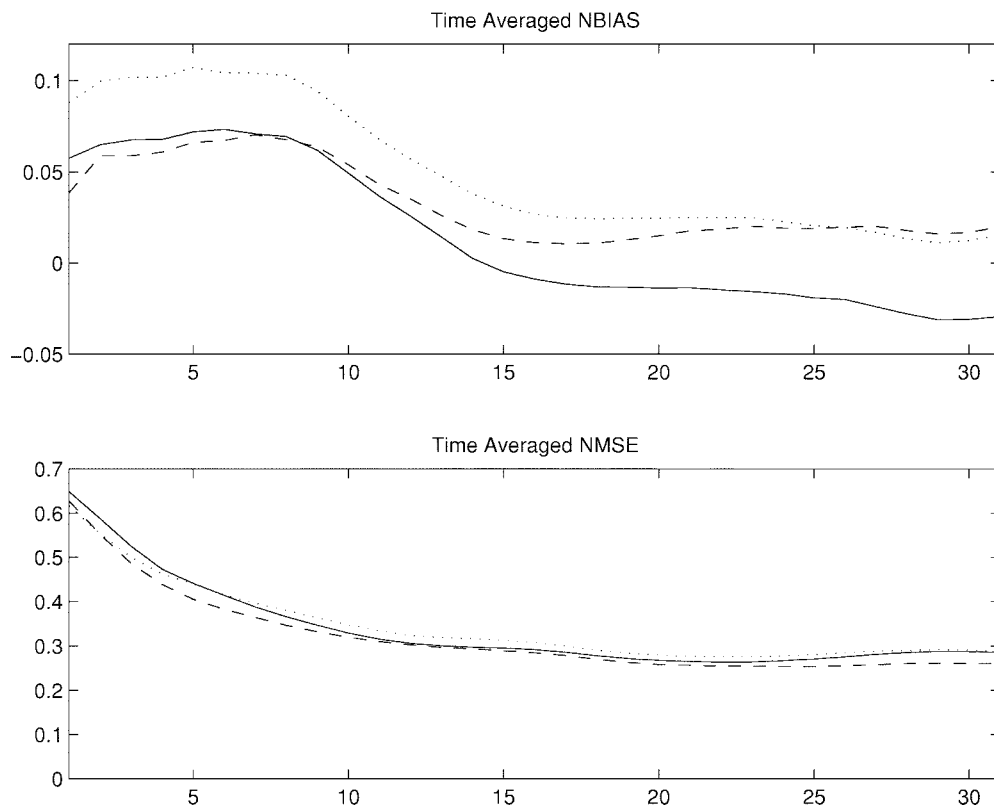|	
Sampling	A uniformly random sampling of the function's parameters domain is performed.
Concentration	The most significant samples (i.e., those providing the smallest values of the

Fig. 13. Time-averaged NBIAS (upper plots) and NMSE (lower plots) for the DRT sequence. Continuous lines: reconstructions not affected by noise. Dashed lines: noise of type a) + c). Dotted lines: noise of type b) + c). Each curve represents the average of 50 DRT reconstructions performed on the same sequence of attenuation measurements.

function) are extracted and subdivided into groups.

Clustering   Groups of samples belonging to different influence zones (referred to as "local minima attraction zones") in the function's parameters domain are recognized.

Local Searches   In each cluster, a local minimum is searched for.

Stopping Criterion   Depending on the results, it is decided whether to stop or continue with further sampling/searches.

The Timmer Algorithm is one of the simplest and most effective algorithms of the clustering methods class [17], [16]. Its objective is to find all local minima that potentially are global minima. We have devised and used a modified version of such an algorithm, referred to as ATA1, which includes an acceptance–rejection law to discard all samples leading to an overestimate of one or more elements of m for the reason explained in the paper.

First, ATA1 uniformly samples the E functional over the search domain A^4. Then, from the set of samples, ATA1 extracts those giving the smallest values of E. Finally, the samples of subsets that are too close to others with a smaller value of E are discarded (notice that this is the peculiarity of Timmer clustering). The concept of "too close" is implemented through the following definition of exclusion distance

threshold

$$r_q = \pi^{-1/2} (\sigma \mu(A) \Gamma(1 + n/2) \, \log(q)/q)^{1/n} \qquad \text{(A1)}$$

where $\Gamma(x)$ is the Gamma function, q the number of samples considered, n the dimension of the search space ($n = 4$ in our case), and $\mu(A)$ the Lebesgue measure of search domain. σ is a predefined parameter. Values between two and four are recommended [17]. If the Euclidean distance between the current sample and any of those not discarded already is smaller than r_q, the current sample is in turn discarded. Our experimental results suggested utilization of an alternative version of ATA1, referred to as ATA2, the only difference being that the acceptance–rejection law is not applied. As explained in the paper, ATA2 is called by the module PSS in case ATA1 fails in finding solutions capable of meeting the ET threshold requirement jointly with the acceptance–rejection law.

Fig. 14 is an example of how PSS works. The PC's are represented as nodes of a search tree. The upper left number in each node is the sequential reference number of the PC, i.e., the number of times that the algorithm of Fig. 5 has been called when that node is reached during the PSS. The lower right label indicates its outcome. The ATA labels mean that PC's were generated by the corresponding algorithm, while Stop labels mean that the corresponding stopping criterion (introduced in Section III-C2) is met. Bold numbers reported below each node indicate the generation sequence. Each branch, made up of all PC's from PC(0) (i.e., the null a) to the PC where one
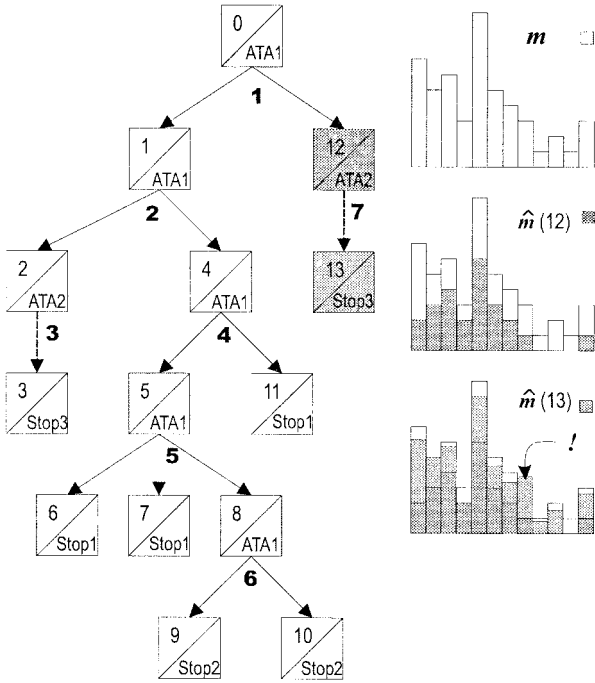
Fig. 14. Sketch of the PSS strategy. PC's are represented by boxes with c/action (*c* is the check order, and "action" corresponds to ATA1, ATA2, or to the end of proliferation of the current branch due to one of the three stopping conditions). Bold numbers indicate the sequence of new PC generation by a given node. PC(0) is the null *a*. On the right of the figure are shown the *m* (white) and *m̂* contributions by PC(12) and PC(13) (evidenced by two different gray levels). The arrow indicates an attenuation overestimate due to ATA2.

of the three stopping criteria is met, forms an RS that will be accepted or discarded. In the example of Fig. 14, the maximum value for N_{PC} is set to five, and the maximum proliferation at each node is set to three PC's. Hence, the following RS's are accepted

$$[\text{PC}(1)\,\text{PC}(4)\,\text{PC}(5)\,\text{PC}(6)];\ [\text{PC}(1)\,\text{PC}(4)\,\text{PC}(5)\,\text{PC}(7)];$$
$$[\text{PC}(1)\,\text{PC}(4)\,\text{PC}(11)]$$

while the others are all discarded.

Initially, ATA (meaning here ATA1 or ATA2 without distinction) is called with *m* as input (stage 0). Let us suppose a first PC set (stage 1) is found, composed of two optimal PC's. A first branch [from PC(1)] is then checked down through a second ATA call applied to the residual attenuation vector obtained by removing the contribution of PC(1). Let us suppose that two new PC's are found [PC(2) and PC(4)]. The residual attenuation vector is updated and ATA is called again, going further down to the PC(3). Here, a stopping condition is met, the corresponding RS is discarded in this case, and processing continues from PC(4).

The right-hand side of Fig. 14 shows the *m* vector components and the contributions to *m̂* by PC(12) and PC(13). The arrow indicates that the attenuation contribution of PC(13), generated by ATA2, causes the overestimate of one of the components of *m*. Therefore, the generation of PC's stops at that stage.

Notice that at the *i*th search stage, the PSS module must define the boundary of the search domain A_i^4. This is a basic

issue for the efficiency of the whole SRT. The PSS module indeed can be initialized by exploiting the statistical parameters associated with *m* and some parameters depending only on the network topology. The basic criteria are mentioned in the paper, but more specific remarks can be made considering the vector *k* of the observed mean specific attenuation, defined by (14). In fact, the mean value and the standard deviation of *k* are immediately exploitable for the adaptive definition of the A_i^4 boundaries.

1) The minimum value $W_{\min}$ that the generic W_i of each PC can take on is calculated through an inverse proportionality law from the normalized standard deviation of *k*. However, $W_{\min}$ can never become smaller than a fixed value, depending on the network topology. For the two networks introduced in Section V, this fixed value is 0.5 and 0.9 km. The upper limit is $W_{\max} = 10\,W_{\min}$ in any case.

2) The outer limits of the PC's centered in the area to be monitored are defined according to $W_{\min}$ so that only PC's with significant contributions to *m* can be considered.

3) The limit values accepted for *s* are related to the ratio between the mean value of *k* and $W_{\min}$ through a linear proportionality law.

A. RSS Module

The task of the RSS module is to eliminate or mitigate the following problems, which are not accounted for by the PSS.

Overlapped PC's: Suppose that at a given stage of the PSS search (e.g., ATA) finds a PC such that further processing, driven by the corresponding residual vector $\bm{m} - \hat{\bm{m}}$, leads to an additional but similar PC in the following stages. The final RS thus contains two PC's that can be merged together without significantly modifying *m̂* and reducing the geometric dimension of the RS by a factor of four. This evidently speeds up the reconstruction process in its final phases.

Inadequate Projection of PC's: Both the PSS and RSO modules may generate PC's whose position makes them not representative. When all distances of a given PC center from the measurement paths exceed a threshold, that PC is not projected properly in *m*. The RSS module directly eliminates such PC's in order to avoid the anomalous behaviors of the RSO module that we experienced.

Similarity of Two or More Reconstructed Fields: This is the most frequent anomaly. It is due to solutions that, while appearing quite different in $A^{4 \times N_{\text{PC}}}$, actually correspond to nearly identical reconstructed rainfall fields. This typically occurs when two solutions are made up by almost identical PC's that are ordered differently. To detect this problem, a comparison among the global reconstructed field solutions is routinely performed, rather than among the possible recombinations of all PC's of all solutions.

The search method based on a rigid separation of the PSS and RSS functions, though appearing somewhat redundant, exhibited much better results in terms of speed than an apparently "smarter" combined algorithm that performed the comparison among the RS's at each stage of PSS. Such a

strategy could be assimilated roughly to a fuzzy clustering technique. In effect, each PC generated in the tree by ATA is kept until the branch generation ends, and the "degree of membership" with respect to a certain family of RS is converted to a binary logical value only when PSS has completed its search. Sets of PC's at intermediate stages of PSS, even if considered similar to each other, might generate other PC's that are radically different (as a consequence of the ATA strategy). Deciding which one is the best RS, as mentioned in this paper, cannot be done simply by checking the way it fits $\boldsymbol{m}$. Therefore, the PSS module has been conceived to operate a preliminary screening, finding the RS's with the highest degree of similarity, followed by the RSS module detection of redundant RS's or PC's. Such a detection is then reiterated, resorting to other evaluation criteria operated through the successive MAS module.

B. RSO Module

The RSO module performs a local minimum search, starting from each current RS. Both simplex and quasi-Newton methods were tested. Since E belongs to C^∞ (see point 1 in Section III-B), problems of convergence never occurred in this simple problem of local minimization.

The RSO module uses the functional E of (13), multiplied by the position functional $B(\boldsymbol{a})$

$$E_b(\boldsymbol{k}, \hat{\boldsymbol{k}}(\boldsymbol{a}), N_P, \boldsymbol{a}) = E(\boldsymbol{k}, \hat{\boldsymbol{k}}(\boldsymbol{a}), N_P) \cdot B(\boldsymbol{a}) \qquad (A2)$$

with

$$B(\boldsymbol{a}) = 1 + \sum_{i=1}^{N_{PC}} \sum_{j=1}^{4} \{ \exp[-w_{ij}(\hat{a}_{ij} - a_{ij})]$$
$$+ \exp[-w_{ij}(a_{ij} - \breve{a}_{ij})] \} \qquad (A3)$$

where a_{ij} is the jth parameter of the ith PC, $\hat{a}_{ij}$ and $\breve{i}j$ are, respectively, the upper and lower limit of its local search domain, and w_{ij} is the parameter expressing the strength of the constraint of that component. Values of w_{ij} proportional to $(\hat{a}_{ij} - \breve{a}_{ij})$ have been adopted so that the contribution of the position functional is preponderant when just one PC parameter falls out of the local search domain, while on the other hand rapidly approaching unity when all PC parameters fall within it.

Notice that the modified functional E_b does not degrade in any way the algorithm's convergence, while it limits abrupt parameter changes with respect to the initial guess. Also, E_b is more profitable than E for the following reason. Since practical measurement networks do not cover the monitored basin uniformly, it is unavoidable that some areas will contribute to E more than others. While the PSS is based on a random criterion, the RSO module is driven only by the error functional. Thus, it may tend to a general reorganization of PC's (to minimize E) by moving them freely in a manner that may not be physically consistent. Instead, the RSO module must only effect the final adjustments to the initial guess by exploring $A^{NPC \times 4}$ closely compared to the current RS.

Finally, notice that the RSS module becomes more effective after the first iteration of SRT since it brings out the similarity

of two separate reconstructed fields to a greater degree, as the RSO module forces them to converge toward similar configurations.

C. MAS Module

As shown in Fig. 4, the MAS module controls both the RSS and RSO. It operates on the whole set of current RS's (both the current stored RS's and the current intermediate RS's), checking whether the RSS and RSO processing has reduced E effectively. In doing this, it accounts for the parameter N_{PC} of each RS, too.

Through a statistical analysis of the whole current RS set, the MAS module decides whether a given RS must be accepted and stored, discarded, or processed again by the RSS and RSO. This acceptance–rejection criterion is based on the trends of E and N_{PC} of each RS found. The RS is accepted if the former parameter decreases, and the latter settles around a fixed value. Then, the accepted RS's finally are stored if their E value is below E_{TF}. Otherwise, further processing is requested of the RSS and RSO. Some search parameters of these modules (e.g., the maximum number of iterations of local search in the RSO and the selection thresholds in the RSS) are adapted, accounting basically for efficiency criteria. For instance, an asymptotical behavior of E, accompanied by a large number of RS still under processing after a number of MAS checks, causes the RSS module to become more selective.

REFERENCES

[1] P. Kumar and E. Foufoula-Georgiou, "A multicomponent decomposition of spatial rainfall fields. 1. Segregation of large- and small-scale features using wavelet transforms," *Water Resources Res.*, vol. 29, no. 8, pp. 2515–2532, 1993.
[2] T. M. Over and V. K. Gupta, "Statistical analysis of Mesoscale rainfall: Dependence of a random cascade generator on large-scale forcing," *J. Appl. Meteorol.*, vol. 33, pp. 1526–1542, Dec. 1994.
[3] J. R. Doviak and D. S. Zrnic, *Doppler Radar and Weather Observation*, 2nd ed. New York: Academic, 1993.
[4] I. Orlanski, "A rational subdivision of scales for atmospheric processes," *Bull. Amer. Meteorol. Soc.*, vol. 56, no. 5, pp. 527–530, 1975.
[5] D. Giuli, A. Toccafondi, G. Biffi Gentili, and A. Freni, "Tomographic reconstruction of rainfall fields through microwave attenuation measurements," *J. Appl. Meteorol.*, vol. 30, no. 9, pp. 1323–1340, 1991.
[6] G. Scarchilli, E. Gorgucci, D. Giuli, L. Facheris, A. Freni, and G. Vezzani, Arno project: "Radar system and objectives," in *Proc. 25th Int. Conf. Radar Meteorology*, Paris, France, June 24–28, 1991, pp. 805–808
[7] R. L. Olsen, D. V. Roger and D. B. Hodge, "The aR^b relation in the calculation of rain attenuation," *IEEE Trans. Antennas Propagat.*, vol. AP-26, pp. 318–329, Mar. 1978.
[8] D. Atlas and C. Ulbrich, "Path- and area integrated rainfall measurement by microwave attenuation in the 1–3 cm band," *J. Appl. Meteorol.*, vol. 16, pp. 1322–1331, Dec. 1977.
[9] R. L. Kashiap and M. C. Mittal, "Picture reconstruction from projection," *IEEE Trans. Comput.*, vol. C-24, pp. 915–923, Sep. 1975.
[10] G. T. Herman and A. Lent, "Iterative reconstruction algorithms," *Comput. Biol. Med.*, vol. 6, pp. 273–294, 1976
[11] R. Gordon, "A tutorial on ART," *IEEE Trans. Nucl. Sci.*, vol. NS-21, no. 1, pp. 78–93, 1974.
[12] D. Giuli, A. Toccafondi, G. Biffi Gentili, A. Freni, S. Yim, T. A. Seliga and K. Aydin, "Tomographic reconstruction of rainfall fields through multiparameter attenuation measurements," in *Proc. 25th Int. Conf. Radar Meteorology*, Paris, France, June 24–28, 1991, pp. 552–555.
[13] S. L. K. Yim, "Tomographic imaging of rainfields from multiparameter microwave propagation measurements," M.S. thesis, Dept. Elect. Eng., Univ. of Washington, Seattle, WA, 1991.
[14] I. Rodriguez-Iturbe and P. Eagleson, "Mathematical models of rainstorm events in space and time," *Water Resources Res.*, vol. 23, no. 1, pp. 181–190, 1987.

[15] K. M. Hanson and G. W. Wecksung, "Local basis-function approach to computed tomography," *Appl. Opt.*, vol. 24, no. 23, pp. 4028–4039, 1985

[16] F. Schoen, "Stochastic techniques for global optimization: A survey of recent advances," *J. Global Optimiz.*, vol. 1, no. 1, pp. 207–228, 1991.

[17] G. T. Timmer, "Global optimization: A stochastic approach," Ph.D. dissertation, Erasmus Univ., Rotterdam, The Netherlands, 1984.

[18] D. Giuli, L. Facheris, and S. Tanelli, "Stochastic technique for 2D tomographic reconstruction of rainfall fields through microwave measurements," in *Proc. Mathematical Methods in Geophysical Imaging IV*, Denver, CO, Aug. 1996, pp. 129–139.

[19] C. Barancourt, J. D. Creutin, and J. Rivoirard, "A method for delineating and estimating rainfall fields," *Water Resources Res.*, vol. 28, no. 4, pp. 1133–1144, 1992.

Luca Facheris (S'92–M'94) received the Laurea (M.S.) degree cum laude in electronic engineering from the University of Florence, Italy, in 1989. He received the Ph.D. degree in electronic and information engineering in 1993 from the University of Padua, Italy.

Since 1993, he has served as an Assistant Professor of telecommunications in the Department of Electronic Engineering, University of Florence. His main research interest is in the area of signal and data processing for active remote sensing, with particular interest in radar polarimetry and ground and spaceborne weather radars.

Dino Giuli (M'82–SM'84) received the Laurea (M.S.) degree in electronics engineering from the University of Pisa, Italy, in 1970.

Since 1973, he has been a Faculty Member of the Department of Electronics at the University of Florence, Italy, where he serves now as Full Professor. His research activity has been devoted primarily to experimental and theoretical research in the field of radar systems. He also is involved in research in digital commuications and telecommunication networks. His current radar research is devoted to optimum processing of dual-polarization radar signals and data and to their integration with data from other spaceborne or ground-based sensors.

Prof. Giuli is a member of the Italian Electrical Association (AEI).

Simone Tanelli (M'99) received the Laurea (M.S.) degree in electronic engineering from the University of Florence, Italy, in 1995, where he is currently pusuing the Ph.D. degree in methods and technologies for environmental monitoring.

He is currently with the Radar and Radiocommunications Laboratory group in the Department of Electronic Engineering, University of Florence. His main research interest is in the area of remote sensing of atmosphere. In particular, his research interests include tomographic inversion problems, spectral analysis of absorption measurements through atmosphere, and weather radar data processing.